ChemCatChem

The European Society Journal for Catalysis

Chemistry Europe

European Chemical Societies Publishing

Supported by

GECATS GERMAN CATALYSIS SOCIETY

Accepted Article

Title: Exploring the Effects Behind the Outstanding Catalytic Performance of PdAg Catalysts Supported on Almond Shell-Derived Activated Carbon Towards the Dehydrogenation of Formic Acid

Authors: Paula Riquelme-García, Jessica Chaparro-Garnica, Miriam Navlani-García, and Diego Cazorla-Amorós

To be cited as: *ChemCatChem* **2024**, e202400160

Link to VoR: https://doi.org/10.1002/cctc.202400160

WILEY VCH

WILEY VCH

RESEARCH ARTICLE

Exploring the Effects Behind the Outstanding Catalytic Performance of PdAg Catalysts Supported on Almond Shell-Derived Activated Carbon Towards the Dehydrogenation of Formic Acid

Paula Riquelme-García, Jessica Chaparro-Garnica, Miriam Navlani-García and Diego Cazorla-Amorós*

[a] P. Riquelme-García, Dr. J. Chaparro-Garnica, Dr. M. Navlani-García and Prof. Dr. D. Cazorla-Amorós
Department of Inorganic Chemistry and Materials Institute
University of Alicante
Ap. 99, Alicante, E-03080, Spain
E-mail: paula.riquelme@ua.es, jessica.chaparro@ua.es, miriam.navlani@ua.es and cazorla@ua.es

Supporting information for this article is given via a link at the end of the document.

Abstract: In this work, highly efficient carbon-supported Pd-based catalysts for formic acid dehydrogenation were synthesized by a straightforward wet impregnation-reduction method. The carbon support was obtained from a biomass residue (almond shell) prepared via H_3PO_4-assisted hydrothermal carbonization (HTC) and thermal activation. This carbon support was doped with nitrogen groups to study the effect on the electronic properties and catalytic performance of the catalysts. Investigating the formation of PdAg alloys with varying Pd:Ag molar ratios resulted in catalysts exhibiting enhanced catalytic activity compared to monometallic Pd counterparts. Notably, the $Pd_1Ag_{0.5}$/NAS catalyst displayed outstanding catalytic performance, achieving an initial TOF of 1716 h^{-1} (calculated in the first 3 minutes of reaction and expressed per mole of Pd) and maintaining substantial activity over 6 consecutive reaction cycles. This work elucidates the successful synthesis of effective catalysts, emphasizing the influence of nitrogen doping and PdAg alloy composition on catalytic behavior and stability.

Introduction

Formic acid (FA), which is the simplest carboxylic acid with a chemical formula HCOOH, has lately received great attention due to its excellent properties as a hydrogen carrier molecule (i.e. high volumetric hydrogen density of 53 g L^{-1}, stability at room temperature, low-toxicity, easy transportation and handling, and safe storage, among others) [1]. FA is classified within the Liquid Organic Hydrogen Carriers (LOHCs), which encompasses a two-step cycle for the hydrogen storage, namely (1) loading/storage of hydrogen (hydrogenation reaction) into the LOHC molecule and (2) unloading/release of hydrogen (dehydrogenation reaction) [2]. In this case, CO_2 would be used as the starting molecule for the generation of FA, which would also contribute to the carbon capture, utilization, and storage (CCUS) technology by converting one of the main greenhouse gases into a valuable molecule that could play an important role in energy transition [3]. Ideally, such a FA-dehydrogenation-CO_2-hydrogenation recycling process implies zero CO_2 emission, which is of great relevance from the environmental point of view and makes FA an outstanding LOHC for practical applications [4].

However, developing suitable catalysts to boost the FA dehydrogenation pathway (HCOOH (l) ↔ H_2 (g) + CO_2 (g)), while avoiding the undesired side dehydration reaction (HCOOH (l) → H_2O (l) + CO (g)), is mandatory to afford the coveted molecular hydrogen. Several types of catalysts have been explored, covering homogeneous catalysts based on metal complexes, supported metal complexes, and heterogeneous catalysts based on metal nanoparticles or single metal atoms loaded on supports of diverse nature [4-7]. Among them, those based on metal nanoparticles supported on carbon materials are one of the preferred options due to the possibility of tailoring the properties of both metal active sites and catalytic supports [1]. As for the metal nanoparticles, Pd is the preferred alternative, since Pd-based catalysts have shown excellent performance for the decomposition of FA in terms of both activity and selectivity towards the desired reaction pathway (i.e. dehydrogenation reaction). However, even better results have been achieved while modulating the features of the Pd active sites by incorporating a second metal in the nanoparticles. In this sense, bimetallic catalysts and, in particular PdAg catalysts, have been fruitfully investigated, achieving very promising results which are normally attributed to the modification of the electronic properties of the Pd centres [4], [8-13]. In the case of the support, it has also been shown that the incorporation of heteroatoms and, in particular, nitrogen functional groups, is a very interesting approach to achieve heterogeneous catalysts with enhanced performance. Such nitrogen atoms have been claimed to be responsible for attaining electron-deficient Pd species, which are needed to boost the dehydrogenation of FA. Also, such nitrogen functional groups have been reported to serve as anchorage sites for the metal species, helping therefore to attain well-distributed metal nanoparticles with sintering resistance under reaction conditions [14]. The diversity of carbon materials has been reflected in the

catalysts used for the dehydrogenation of FA. Heterogeneous catalysts supported on activated carbon [15-18], carbon nanotubes [19-22], mesoporous carbons [23-26], carbon nitride [27-29], etc. have been reported in the recent literature. We have recently explored the performance of activated carbon prepared from lignocellulosic biomass residues such as hemp [14, 31] and almond shells [32]. The use of such residues to develop catalysts that are used for the production of H_2 from FA is an overall approach that is well aligned with the principles of the circular economy and can be encompassed in a process that addresses important aspects for future sustainable scenarios. In this case, almond shell was selected as the biomass precursor because of its high carbon content and low ash content, which makes it an excellent option for obtaining porous carbons with well-developed textural properties [33]. Moreover, in our research group, this biomass has been extensively studied in such a way that the conditions to control the textural properties have been optimized [32], [34-36]. Also, it is important to notice that almond biomass is very abundant in our geographical region, which reduces the cost and environmental impact that using other biomass sources would have.

The interesting results motivated us to further explore the potential of such biomass residues and, in this study, we aimed to design biomass-derived carbon-supported catalysts by considering the following aspects: (1) the composition of PdAg nanoparticles in the catalysts and (2) the presence of nitrogen functional groups in the support.

Results and Discussion

The measurements of the pH_{pzc} indicated the acid-base character of the carbon supports. The AS support presented an acid pH_{pzc} of 4.8, while NAS support had a pH_{pzc} of 5.6, which can be explained by the basic character of the incorporated nitrogen groups.

The results of the N_2 adsorption-desorption isotherm indicated that both AS and N-AS showed a sharp N_2 uptake at low relative pressures, typical of microporous materials. A hysteresis loop was also seen, which is related to the presence of mesopores, which indicated that both supports had a combination of Type I and IV isotherms (See Figure S1). The apparent surface area (S_{BET}) and micropore volume (V_{DR} N_2) of the AS was not significantly affected after the incorporation of the nitrogen functional groups (2010 m^2/g and 0.76 cm^3/g, and 1980 m^2/g and 0.75 cm^3/g, for AS and NAS, respectively).

Figure 1 displays the TEM micrographs of all the catalysts together with the histograms with the distribution of the nanoparticle size. The average nanoparticle size is included in Table 1 together with the Pd loading determined by ICP analysis. As can be seen in Figure 1, monometallic Pd nanoparticles are well-distributed in both Pd/AS and Pd/NAS catalysts, and they have an average nanoparticle size of 3.8 and 3.2 nm, respectively. In the AS-supported bimetallic catalysts, the particle size is influenced by the composition of the Pd-Ag nanoparticles. It is observed that the addition of Ag slightly increases the average particle size with respect to the monometallic catalyst (average size of 4.5, 4.0, 4.1, and 5.0 nm, for $Pd_1Ag_{0.3}$/AS, $Pd_1Ag_{0.5}$/AS, $Pd_1Ag_{0.7}$/AS, and Pd_1Ag_1/AS, respectively), but finding a relationship between the composition of the nanoparticles and their average size is not straightforward because the atomic rearrangement in the nanoparticles might differ. However, the particle size of NAS-supported bimetallic catalysts is smaller concerning the respective monometallic catalyst and does not depend on the Ag composition (average size of 2.7, 2.8, 2.7, and 2.8 nm, for $Pd_1Ag_{0.3}$/NAS, $Pd_1Ag_{0.5}$/NAS, $Pd_1Ag_{0.7}$/NAS, and Pd_1Ag_1/NAS, respectively). This is due to the fact that the nitrogen groups of the NAS support serve as anchoring sites for Pd and Ag species during the nanoparticles formation, thereby affording smaller and well-distributed bimetallic nanoparticles. The effect of nitrogen groups on the average particle size is most evident in bimetallic catalysts, such that the average size of the nanoparticles comparing the AS and NAS-based catalysts decreased by ~16 % for the monometallic samples, while such a decrease was 40, 30, 34, and 44 % for $Pd_1Ag_{0.3}$, $Pd_1Ag_{0.5}$, $Pd_1Ag_{0.7}$, and Pd_1Ag_1 catalysts, respectively.

As for the Pd content, ICP results (Table 1) evidenced that it was very close to the nominal loading for all the catalysts (1 wt%).

XPS analysis of the support (Figure S2) indicated that the N functional groups are in the form of pyridone/pyrrole (19%), amine/amide (47%), and pyridine groups (34%). The electronic properties of the metal species were also analyzed by XPS. It is well known that Pd 3d spectra display two signals that correspond to Pd $3d_{5/2}$ and Pd $3d_{3/2}$ (at lower binding energies and higher binding energies, respectively) electron transitions, and each of them can be deconvoluted in contributions that correspond with Pd species with different electronic properties. As indicated in Figure 2(a), such Pd species correspond to Pd^{2+} and Pd^0 in the developed catalysts. It can be observed in the Pd spectra, and also in Table 1, that the relative proportion of Pd^{2+} and Pd^0 depends on the composition of the samples. In this sense, it has been observed that the N-containing catalysts have a more significant contribution of Pd^{2+} species than the counterpart N-free catalysts, which is attributed to the participation of N functional groups stabilizing the Pd^{2+} species, which has already been reported in our previous studies [19, 32]. It should be also noted that the position of the peaks reveals the presence of Pd species with different electronic properties. The peak positions of the Pd^0 and Pd^{2+} species present in the NAS-supported catalysts undergo a small shift towards higher binding energies due to the effect of the N-groups on those samples compared to AS-supported counterparts. In the case of monometallic catalysts, this shift effect is more pronounced (the Pd^0 $3d_{5/2}$ peaks appear at 335.6 and 336.0 eV and the Pd^{2+} $3d_{5/2}$ peaks appear at 337.5 and 338.0 eV, for Pd/AS and Pd/NAS, respectively) than in the bimetallic samples, which is due to the presence of “bare” Pd species directly interaction with the N atoms present in the support. Due to the complexity of the catalytic system, and hence the multiple electronic effects, in this work, unlike other studies [37-39], Ag incorporation did not modify the position of the peaks displayed in the Pd XPS spectra, what can be due to counteracting effects of alloy formation and interaction with the carbon support.

Figure 2(b) shows the Ag 3d XPS spectra and it can be observed that, unlike the Pd spectra, the Ag monometallic catalysts exhibit

10.1002/cctc.202400160

a negligible peak shift between AS-supported and NAS-supported samples (368.2 and 374.1 eV, Ag $3d_{5/2}$ and Ag $3d_{3/2}$, respectively) compared to the bimetallic catalysts. Concerning the bimetallic catalysts, the presence of Pd produces a shift of ~ 0.4 eV towards lower binding energies for the AS-supported catalysts, while in the case of NAS-supported catalysts, this change in binding energy is smaller reflecting the electronegative character of the N-groups in charge redistribution. Therefore, considering the results obtained from the XPS spectra, it might be concluded that in the PdAg catalysts Ag species are enriched in electronic charge. However, this fact is not in agreement with the difference in electronegativity of the metals (2.2 and 1.9, according to the Pauling scale, for Pd and Ag, respectively), according to which one would expect Pd to gain electron density and Ag to lose it. Such an apparent discrepancy with the generally accepted trend was explained in the work of Coulthard and Sham about the charge redistribution in Pd-Ag alloys [40]. Those authors claimed that both Pd and Ag gain d-charge when both metals are forming alloys and that such charge gain is compensated by a loss of non-d charge (s or p). The d-charge gain of Ag is in good agreement with the shift towards lower binding energies that is observed in PdAg samples [40], while that effect is not as evident in Pd spectra due to the effective interaction with the support which seems to affect in a larger extent to the Pd atoms.

In summary, XPS analysis and TEM show that both the interaction with the support and the alloy with Ag produces interesting changes in the Pd electronic structure and particle size that have an important impact in the catalytic activity (*vide infra*).

Table 1. Results of the characterization of the samples.

Catalyst	Average diameter / nm	ICP	XPS	
		Pd total wt%	Pd^{2+} / %	Pd^{0} / %
Pd/AS	3.8 ± 2.1	0.7	9.7	90.3
Pd/NAS	3.2 ± 0.9	0.8	39.1	60.1
$Pd_1Ag_{0.3}$/AS	4.5 ± 0.9	1.1	9.4	90.6
$Pd_1Ag_{0.3}$/NAS	2.7 ± 0.7	0.9	30.3	69.7
$Pd_1Ag_{0.5}$/AS	4.0 ± 1.3	1.0	4.3	95.7
$Pd_1Ag_{0.5}$/NAS	2.8 ± 1.1	1.2	65.0	35.0
$Pd_1Ag_{0.7}$/AS	4.1 ± 1.2	0.9	15.2	84.8
$Pd_1Ag_{0.7}$/NAS	2.7 ± 0.6	0.9	45.2	58.2
Pd_1Ag_1/AS	5.0 ± 2.0	0.8	0	100
Pd_1Ag_1/NAS	2.8 ± 0.5	0.8	51.7	48.3

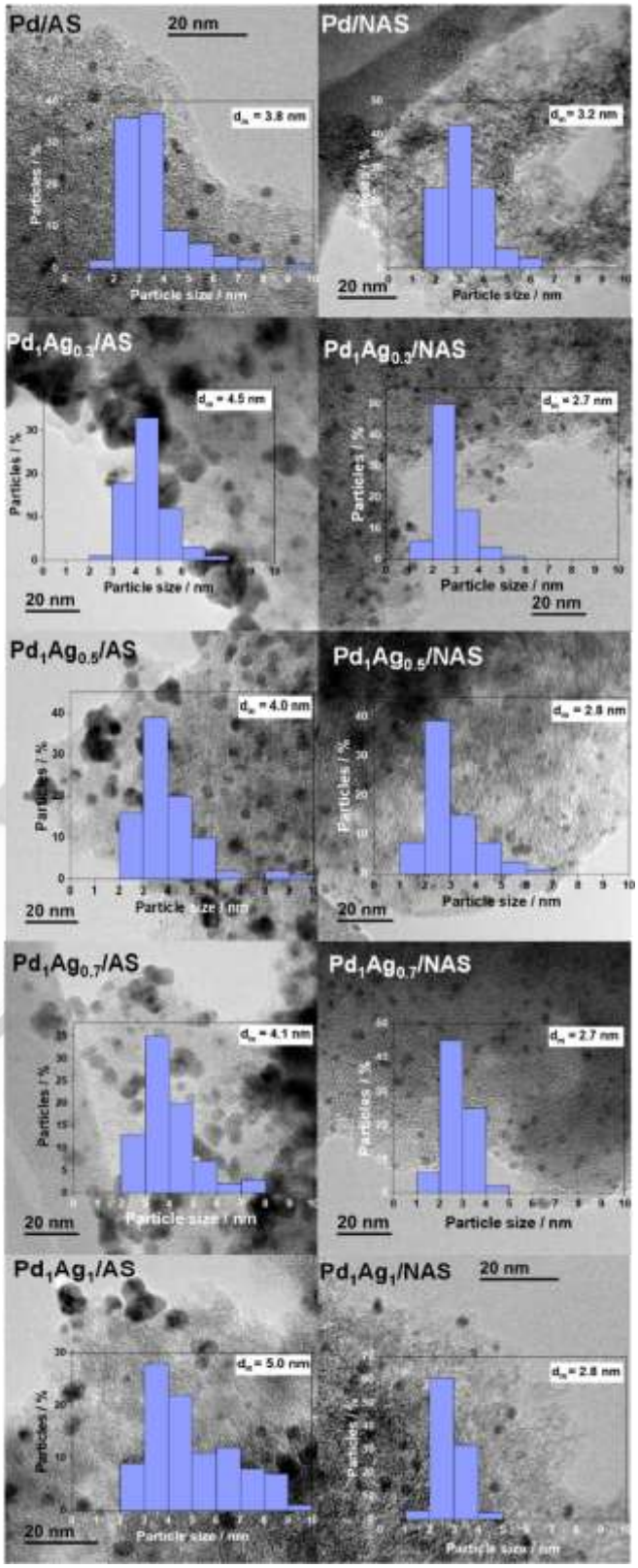

Figure 1. TEM micrographs and histograms with Pd and PdAg nanoparticle size distributions.

Figure 3 depicts the profiles of gas generated (H_2 + CO_2) from the decomposition of FA by monometallic Pd and bimetallic PdAg catalysts with different compositions. The results of the monometallic Ag samples are also included for comparison

purposes. As can be seen in those profiles, none of the samples had an induction time and the gas evolved from the beginning of the monitored reaction time. However, important differences can be seen when comparing the performance of the samples. In this sense, a significant enhancement of the catalytic activity was achieved for all the PdAg catalysts compared with the monometallic samples, reaching much larger volumes of gas for both AS and NAS-supported catalysts. It was observed that, in both sets of samples (i.e. AS-supported and NAS-supported catalysts), the total volume of gas generated was strongly dependent on the composition of the nanoparticles and, among investigated, it was maximum for those samples with a Pd/Ag molar ratio of 1/0.5.

The positive effect of the incorporation of Ag to the Pd-based catalysts used to boost the decomposition of FA has been previously observed in other studies [10, 32, 11] and it is usually attributed to the modification of electronic properties of Pd species or the increased resistance against CO-poisoning [8]. However, such conclusions are not that straightforward when a new component, such as nitrogen functional groups in this study, is present in the catalysts, since the features of Pd species may be modified by the presence of both Ag and N in the catalysts. In this sense, it has been observed that those NAS-supported catalysts have a much larger contribution of Pd^{2+} species than the N-free samples, for all the studied compositions of the nanoparticles, which has been demonstrated to play a positive role in the performance of the catalysts prepared in this study and also in previous cases [14, 21, 41].

Nevertheless, such a positive effect of the presence of nitrogen functional groups may not be limited to the modification of the electronic properties of Pd active sites, but also some additional effect may be taking place. The following additional effects should not be ruled out: (1) Effect of nitrogen in attaining smaller nanoparticles than those observed in the N-free samples; (2) N-functional groups may modify the basicity of the surface of the catalysts. All these effects may be happening in the studied samples. As for the size of the nanoparticles, TEM analysis evidenced the presence of smaller nanoparticles in the N-containing catalysts compared to the N-free counterpart for both monometallic Pd and bimetallic PdAg samples, achieving a significant reduction in these last samples (~16 % for the monometallic Pd samples, and 40, 30, 34, and 44 % for $Pd_1Ag_{0.3}$, $Pd_1Ag_{0.5}$, $Pd_1Ag_{0.7}$, and Pd_1Ag_1 catalysts, respectively). Such smaller nanoparticles present in N-containing catalysts result in higher atom efficiency and, thus, catalysts with a larger proportion of surface active sites and hence enhance catalytic activities. Concerning the modification of the basicity of the surface of the samples, it may increase upon the incorporation of nitrogen functional groups, which has already been demonstrated for similar catalysts [4]. Such an increase in the basicity of the surface of the samples may favour the interaction of the acidic HCOOH molecules with the samples, hence increasing the local concentration of HCOOH close to the catalytic active centres.

In order to clearly show the positive effect of both Ag in the nanoparticles and nitrogen functional groups in the support, the total volume of gas generated by all the catalysts is shown in Figure 4. It can be seen that there is a volcano-type relationship between the total volume of gas produced from the decomposition of FA and the Ag content in the samples, with the maximum for those $Pd_1Ag_{0.5}$ catalysts (reaching a total volume of gas of 191 and 218 mL for $Pd_1Ag_{0.5}$/AS and $Pd_1Ag_{0.5}$/NAS, respectively, after 30 min of reaction at 75 ºC). The beneficial effects of the presence of nitrogen functional groups can be also seen by comparing the total volume of gas generated by AS-supported catalysts (35, 99, 191, 95 and 112 mL, for Pd/AS, $Pd_1Ag_{0.3}$/AS, $Pd_1Ag_{0.5}$/AS, $Pd_1Ag_{0.7}$/AS, Pd_1Ag_1/AS, respectively) and NAS-supported samples (91, 120, 218, 156, 148 mL, for Pd/NAS, $Pd_1Ag_{0.3}$/NAS, $Pd_1Ag_{0.5}$/NAS, $Pd_1Ag_{0.7}$/NAS, Pd_1Ag_1/NAS, respectively).

10.1002/cctc.202400160

RESEARCH ARTICLE

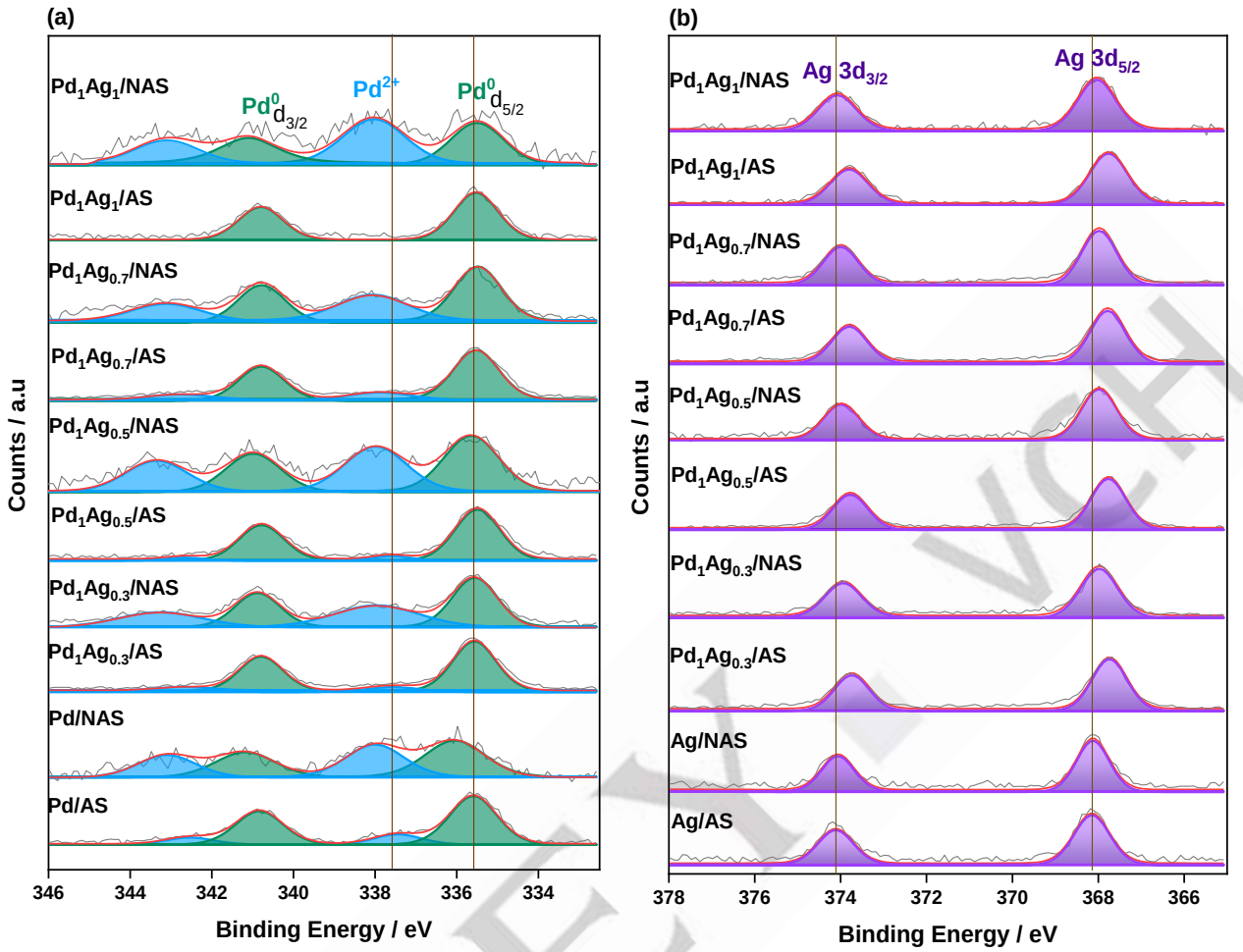

Figure 2. (a) Pd 3d XPS spectra and (b) Ag 3d XPS spectra of the catalysts.

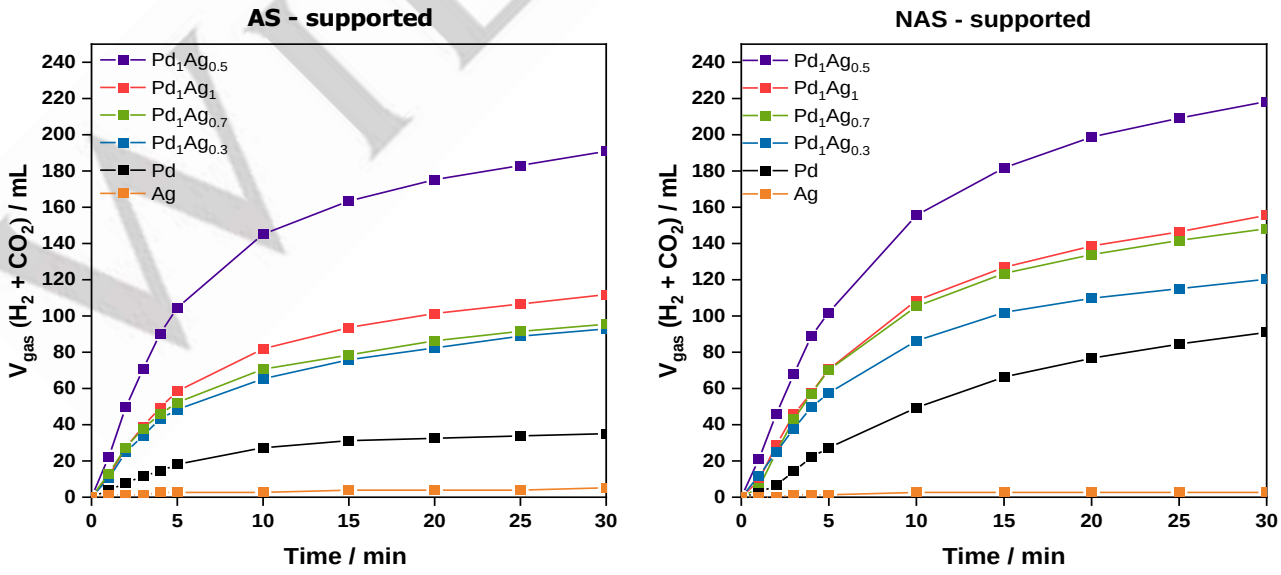

Figure 3. Gas evolution profiles achieved by AS-supported and N-AS-supported catalysts at 75 ºC.

10.1002/cctc.202400160

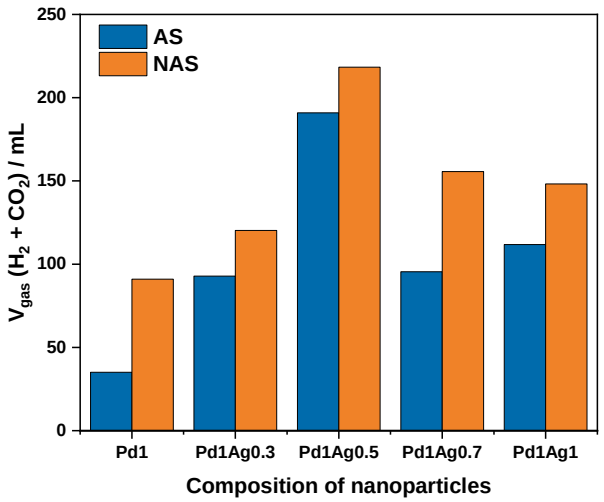

Figure 4. Total volumes of gas generated by the catalysts assessed in the decomposition of FA at 75 ºC after 30 min of reaction.

Among the mentioned features of the catalysts that may play an important role in determining their performance, the presence of Pd species with certain electronic properties should be underlined. In this sense, it is known that the presence of both electron-deficient and electron-rich Pd species is needed to efficiently boost the dehydrogenation of FA following the more plausible reaction mechanism that proceeds *via* the formation of formate intermediate. Such reaction mechanism, which is schematized in Figure 5, encompasses the following reaction steps: (1) Adsorption of formate ion on the surface of Pd nanoparticles, (2) cleavage of the C-H bond of the adsorbed formate ion, and (3) release of H_2 and the regeneration of the catalyst. According to such a plausible reaction mechanism, the presence of both electron-deficient and electron-rich Pd species would be needed, since they would favour the first and second reaction step, respectively [11, 42]. That could be the main reason for the enhanced activity depicted by the N-containing catalysts, which, aside from the electron-rich Pd species (in the form of metal Pd species), have a significant contribution of Pd^{2+}.

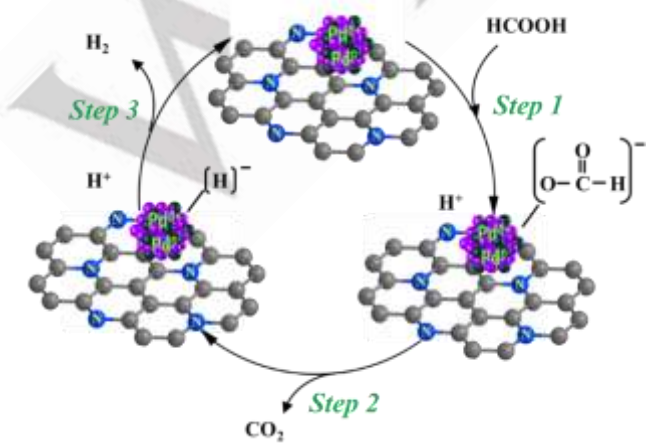

Figure 5. Plausible reaction mechanism for the dehydrogenation of FA.

To get further insight into that effect, the relative proportion of Pd^{2+}/Pd^0 species on the surface of the samples and the initial TOF values achieved by AS and NAS-supported catalysts are plotted in Figure 6. It can be seen that the relative proportion of Pd^{2+}/Pd^0 species on the surface of the samples is very similar for all the AS-supported catalysts, and the presence of Pd^{2+} may be mainly due to the exposure of the samples to the ambient conditions. However, such a relative proportion is not the same for all the NAS-supported samples, which can be attributed to the effect of the N functional groups on the electronic properties of Pd species. It is seen in NAS-supported samples that the $Pd_1Ag_{0.5}$ catalyst, which is the best-performing sample, has the largest relative proportion of Pd^{2+}/Pd^0, which would be in agreement with the positive role of Pd^{2+} species. Such a larger proportion of Pd^{2+}/Pd^0 in $Pd_1Ag_{0.5}$/NAS catalyst may indicate that the Pd-N interaction is more effective for that composition of the PdAg nanoparticles, but further evidence would be needed. As observed in Figure 6, for all PdAg/NAS, the larger the relative proportion of Pd^{2+}/Pd^0, the higher the initial TOF value achieved by the catalyst, regardless of the composition of the nanoparticles, but such a tendency is not followed by the monometallic counterpart since other effects (such as the composition of the nanoparticles and the average nanoparticle size) may be taking place.

10.1002/cctc.202400160

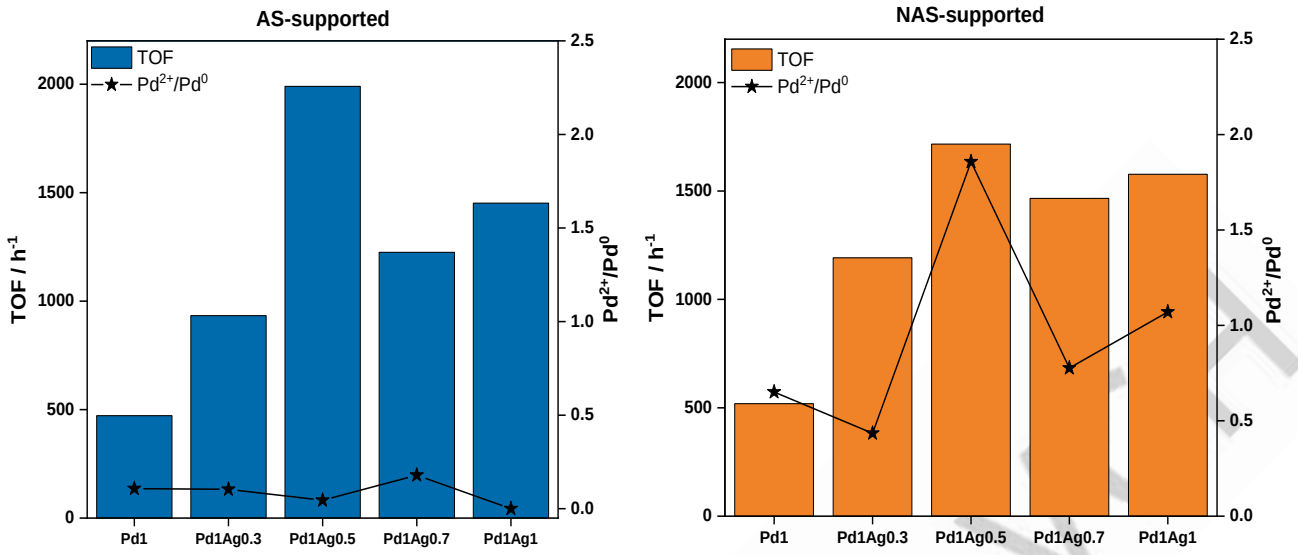

Figure 6. Relationship between the initial TOF (h^{-1}) achieved by both series of catalysts and the Pd^{2+}/Pd^0 relative proportion on the surface of the samples.

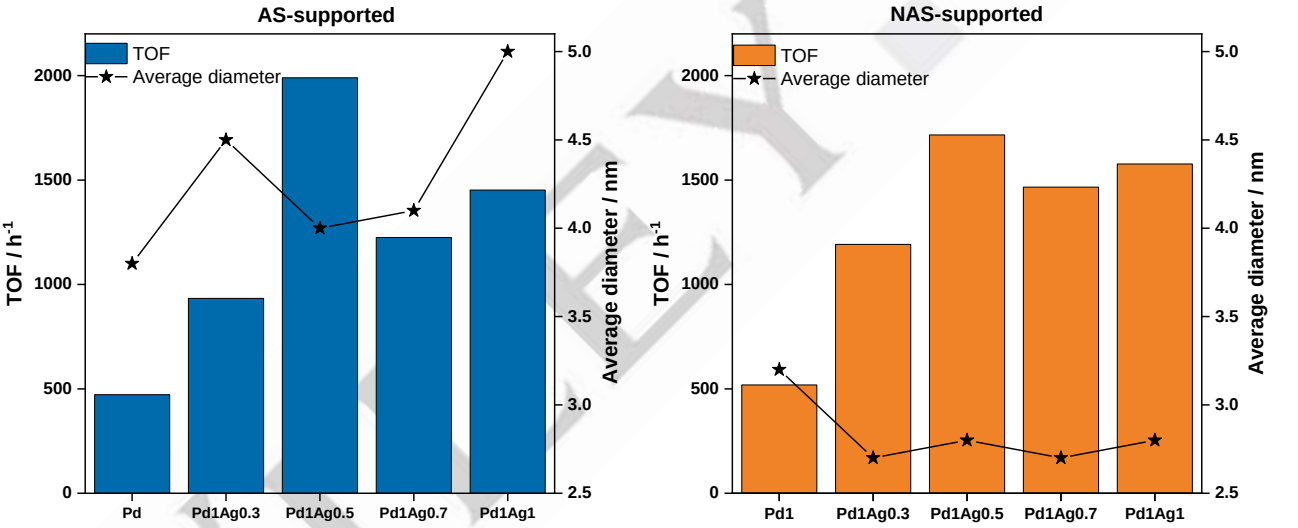

Figure 7. Relationship between the initial TOF (h^{-1}) achieved by both series of catalysts and the average size of the nanoparticles in the samples.

It should be noted that the complexity of the studied materials, which are based on catalysts with various compositions of the nanoparticles and also with and without nitrogen functional groups, hampers somehow the drawing of straightforward conclusions on the main features of the catalysts that determine the performance of the samples. In this sense, the electronic properties of the Pd nanoparticles may seem to be the principal aspect responsible for the catalytic performance of the developed materials, but the effect of other aspects such as the size of the nanoparticles well merits a discussion. For that, the relationship between the initial TOF values, calculated after 3 min of reaction, and the average size of the nanoparticles determined by TEM analysis is depicted in Figure 7 for both series of samples (AS-supported and NAS-supported catalysts). As can be seen, there is not a direct relationship between both parameters, but the samples with smaller average nanoparticle sizes tend to show higher TOF values, which is especially clear for those NAS-supported catalysts. Nevertheless, electronic properties of Pd atoms seem to prevail.

To further assess the performance of the developed materials, the stability of the best-performing catalysts ($Pd_1Ag_{0.5}$/AS and $Pd_1Ag_{0.5}$/NAS) was evaluated by conducting six consecutive reaction cycles, and the results of the gas evolution profiles are included in Figure 8. As can be seen, both samples are still active after six catalytic reaction cycles, but a catalytic activity decay (in terms of volume of gas generated) was observed in both cases, which corresponds to a loss of 57 and 25 % of the initial activity of the catalysts in the sixth reaction cycle compared to the first reaction cycle, for $Pd_1Ag_{0.5}$/AS and $Pd_1Ag_{0.5}$/NAS, respectively.

10.1002/cctc.202400160

RESEARCH ARTICLE

According to that, the stability of the NAS-supported catalysts under reaction conditions is much better than that of the N-free counterpart catalysts. That is also in good agreement with the preserved initial reaction rate observed for $Pd_1Ag_{0.5}$/NAS sample along the cycles (22.7, 20.5, 19.6, 20.0, 17.4, and 17.0 mL min^{-1} for cycles 1 to 6, respectively), while the initial reaction rate shown by $Pd_1Ag_{0.5}$/AS catalyst significantly decreased along the cycles (23.5, 19.6, 17.9, 12.6, 12.2, and 10.0 mL min^{-1} for cycles 1 to 6, respectively). Regarding the stability of the monometallic samples (Pd/AS and Pd/NAS), they are also active after 6 consecutive cycles and the stability of Pd/NAS was better than that of Pd/AS, again highlighting the positive effect of the nitrogen groups and the suitability of the support derived from almond shell residues.

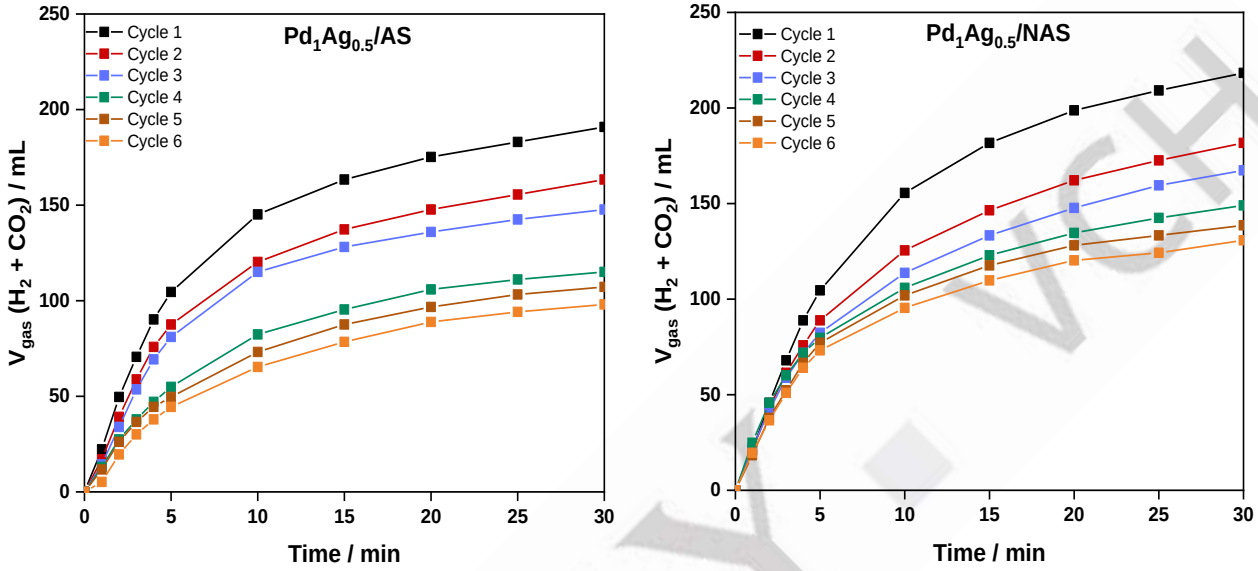

Figure 8. Gas generation profiles attained by $Pd_1Ag_{0.5}$/AS and $Pd_1Ag_{0.5}$/NAS catalysts along six consecutive reaction cycles at 75 ºC.

In order to deepen into the possible reasons responsible for the deactivation of the catalysts, the spent samples were characterized by means of ICP-OES, TEM (Figure 9), XPS (Figure 10), and XRD (Figure S3) after the six consecutive reaction cycles performed. The results of ICP-OES of the used $Pd_1Ag_{0.5}$/AS and $Pd_1Ag_{0.5}$/NAS catalysts demonstrated that there is no loss of Pd during the reaction, indicating that the partial activity decay along the consecutive reaction cycles is not due to Pd leaching. As for the TEM analysis, the micrographs registered for $Pd_1Ag_{0.5}$/AS catalyst indicate the presence of larger nanoparticles and wider particle size distribution than the NAS-supported catalyst, which is evidenced in both fresh and used samples. The increase of the average size of the nanoparticle was 55 and 39% for $Pd_1Ag_{0.5}$/AS and $Pd_1Ag_{0.5}$/NAS, respectively, again confirming the sintering resistance of the NAS-supported materials due to the anchorage effect of the N-functional groups [11,14, 19, 41, 43-45]. Such an increase in the average size of the nanoparticles may be one of the reasons that could explain the deactivation of the catalysts.

Concerning XPS results, it was observed that Pd species were completely reduced to Pd^0 under reaction conditions in the spent $Pd_1Ag_{0.5}$/AS, while the presence of Pd^{2+} species was still detected in the spent NAS-supported counterpart catalyst. The reduction of such species may be caused by the H_2 generated in the decomposition of FA and, considering the importance of Pd^{2+} in the reaction, might be also responsible for the activity decay observed in both cases.

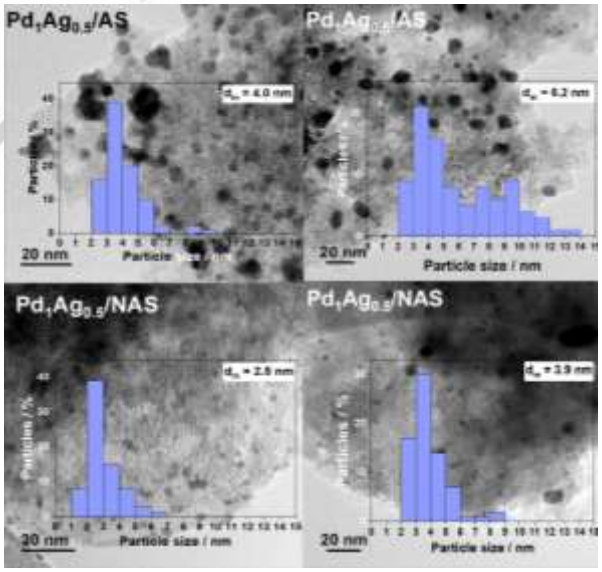

Figure 9. TEM micrographs and histograms of the fresh and used $Pd_1Ag_{0.5}$/AS and $Pd_1Ag_{0.5}$/NAS catalysts.

10.1002/cctc.202400160

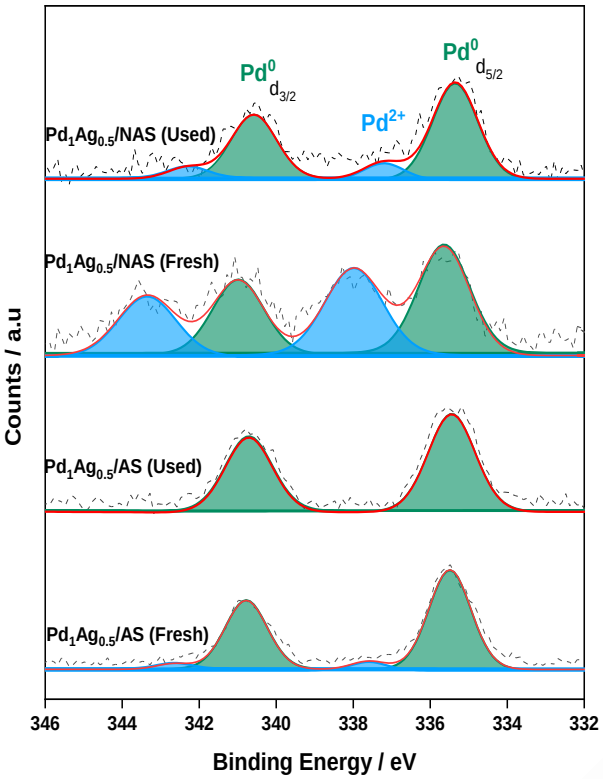

Figure 10. Pd 3d XPS spectra of fresh and used $Pd_1Ag_{0.5}$/AS and $Pd_1Ag_{0.5}$/NAS catalysts.

To get information about the possible changes that the samples may experience during the reaction, XRD patterns were registered for the fresh and used catalysts (Figure S3). The first broad signal appearing in all samples at approximately 24º corresponds to the carbon support. Between the fresh and used $Pd_1Ag_{0.5}$/AS samples no differences in structures are found and the signals at 38.4º and 44.4º could be associated with the PdAg alloy [46,47]. However, differences can be observed between the fresh and used $Pd_1Ag_{0.5}$/NAS sample. In the pattern of fresh $Pd_1Ag_{0.5}$/NAS, the signals at 38º, 44º, 64º and 77º correspond to the (111), (200), (220), (311), (222) Ag crystalline facets, respectively [48,49] while such signals are not present in the pattern of the used sample, in which those signals that correspond to the PdAg alloy (38.4º and 44.4º) are present. The presence of those signals of Ag phases in the fresh $Pd_1Ag_{0.5}$/NAS may be related to the higher amount of Pd^{2+} in that sample compared to fresh $Pd_1Ag_{0.5}$/AS, due to the interaction with the nitrogen groups, which could prevent the complete formation of the PdAg alloy. It can be extracted that the NAS-supported sample experiences a change during the reaction since under the reducing environment caused by the formation of H_2 part of the Pd^{2+} is reduced to Pd^0 (as shown in Figure 10), allowing the formation of the PdAg alloy, which is reflected in the XRD pattern observed for the used $Pd_1Ag_{0.5}$/NAS catalyst.

In order to compare the performance of the developed materials with those reported in the literature, the results of some representative PdAg catalysts used for the dehydrogenation of FA have been included in Table 2. It should be mentioned that among all the catalysts studied, the catalyst prepared in this study, $Pd_1Ag_{0.5}$/NAS, shows very promising results in terms of TOF, and also in terms of stability, which has been assessed during six consecutive reaction cycles.

Table 2. Results of the catalytic performance of representative PdAg catalysts.

Catalyst	Temperature/ ºC	Additive	TOF (h^{-1})	Nº cycles	Ref.
$Pd_1Ag_{0.5}$/NAS	75	HCOONa	1716[b]	6	This work
Pd_1Ag_2/C	75	HCOONa	855[b]	-	[9]
Pd_7Ag_3/CNT	30	HCOONa	928[c]	-	[39]
$Ag_{0.1}$-$Pd_{0.90}$/rGO	25	HCOONa	156[c]	-	[50]
$Ag_{74}Pd_{26}$/graphene	60	HCOONa	572[c]	3	[51]
Ag_1Pd_2/CN	75	-	621[c]	4	[52]
PdAg@ZrO_2/C	50	HCOOK	9206[a][c]	2	[53]
Ag_1@Pd_1/N-GCNT	25	-	413[a][c]	4	[21]
Ag_1Pd_9–MnO_x/carbonspheres	50	HCOOK	3558[a]	5	[54]
PdAg/amine-MSC	75	HCOONa	5638[b]	3	[26]
Ag_9Pd_{91}/g-C_3N_4	50	HCOONa	480	3	[55]
Ag_1Pd_9@NPC	50	HCOONa	3000[a][c]	5	[56]
Ag_1Pd_9/SBA-15-Amine	50	HCOONa	964[c]	5	[28]
PdAg-MnOx/N-SiO_2	40	-	1430[b]	5	[57]
$Ag_{20}Pd_{80}$@MIL-101	80	HCOONa	848[a][c]	-	[58]
Ag_1Pd_4@NH_2–UiO-66	80	-	893[a][c]	5	[59]

[a] Final TOF. [b] TOF expressed per total mole of Pd. [c] TOF expressed per total mole of metal.

Conclusion

Biomass-residue-derived activated carbon-supported catalysts for the production of hydrogen from the formic acid dehydrogenation reaction have been developed in this study. The effect of both the composition of PdAg nanoparticles and the presence of nitrogen functional groups in the support have been checked. It was observed that the presence of both Ag and nitrogen functional groups resulted in catalysts with enhanced performance compared to the monometallic Pd catalysts supported on the N-free activated carbon, which might be related to several aspects such as the modification of the electronic properties on the surface of the Pd species and the presence of particle with and adequate particle size. Among the investigated materials, $Pd_1Ag_{0.5}$/NAS sample displayed the most promising results, with an initial TOF number of 1716 h^{-1} and a relatively high stability during six consecutive reactive cycles. The results herein reported evidence the potential of PdAg alloys and the activated

carbons derived from biomass residues in attaining new sustainable heterogeneous catalysts with tunable properties for their application in reactions of great environmental relevance.

Experimental

Synthesis of the catalytic supports

The catalytic supports used in the present study were based on activated carbon and nitrogen-doped activated carbon, which were synthesized from lignocellulosic biomass residues, namely almond shells (AS), by H_3PO_4-assisted HydroThermal Carbonization (HTC) and using the protocol described in our previous study [32]. The resulting support was denoted as "AS". The incorporation of nitrogen function groups was performed through an organic reaction under mild conditions following the procedure described elsewhere [32]. The N-containing support was denoted as N-AS.

Synthesis of the catalysts

From AS and NAS supports, monometallic (Pd) and bimetallic (PdAg) catalysts were synthesized by standard impregnation followed by reduction with $NaBH_4$ (metal/$NaBH_4$ molar ratio of 1/5) and using $Pd(OAc)_2$ and $AgNO_3$ as metal precursors. A co-impregnation of both metal precursors was used for the bimetallic PdAg samples, using the experimental procedure described elsewhere [32]. All the catalysts had a nominal Pd content of 1 wt% and several Pd/Ag molar ratios were used for the synthesis of the bimetallic samples ($Pd_1Ag_{0.3}$, $Pd_1Ag_{0.5}$, $Pd_1Ag_{0.7}$, Pd_1Ag_1). The monometallic Ag catalysts were also synthesized as references. The as-synthesized catalysts were denoted as follows: Pd/AS, $Pd_1Ag_{0.3}$/AS, $Pd_1Ag_{0.5}$/AS, $Pd_1Ag_{0.7}$/AS, Pd_1Ag_1/AS, and Ag/AS for the N-free catalysts, and Pd/NAS, $Pd_1Ag_{0.3}$/NAS, $Pd_1Ag_{0.5}$/NAS, $Pd_1Ag_{0.7}$/NAS, Pd_1Ag_1/NAS, and Ag/NAS for the N-containing samples.

Characterization

The pH at the point of zero charge (pH_{pzc}) was measured to evaluate the acid-base character of the AS and NAS supports. The procedure was carried out by mixing a specified quantity of each activated carbon support, previously dried in an oven at 110 ºC, with a fixed volume of ultrapure water. This mixture was continuously stirred for 24 hours at 25 ºC [60]. Subsequently, the activated carbon was filtered, and the pH was determined using a pH meter, specifically the MM 374 Hach sensIONTM + multimeter.

Both AS and N-AS supports were characterized by physical adsorption-desorption of N_2 at -196 ºC to get information on their porous texture. An automatic adsorption system (Micromeritics ASAP 2020 analyzer) was used and the samples were degassed at 200 ºC for 6 h before the analysis. The apparent surface area (S_{BET}) and total micropore volume (V_{DR} N_2) were calculated by applying the Brunauer-Emmett-Teller (BET) method and the Dubinin-Radushkevich (DR) equation to the N_2 adsorption isotherm at -196 ºC, respectively. Transmission Electron Microscopy (TEM) was used to get information on the morphology of the catalysts. A JEOL (JEM-2010) transmission electron microscope operating at 200 kV was used and the average size of the nanoparticles was estimated by measuring ~ 100 individual nanoparticles using the ImageJ software. Metal contents were determined by Inductively Coupled Plasma-Optical Emission Spectroscopy (ICP-OES) using a Perkin-Elmer Optima 4300 system. X-ray photoelectron spectroscopy (XPS) analysis was carried out in a VG-Microtech Multilab 3000 spectrometer equipped with a semispherical electron analyzer and a Mg Kα (hv = 1253.6 eV) 300 W X-ray source. Binding energies were referred to the C 1s line at 284.6 eV in all cases.

X-ray diffraction (XRD) analysis was carried out at room temperature with a Bruker X-ray Diffractometer (D8-Advance model) provided with a Göebel mirror and a Kristalloflex X-ray generator (K 760-80F model) with Cu Kα radiation and a scanning rate of 1°/min, in the range of 10–80º.

Catalytic test

The dehydrogenation of FA was performed in the liquid phase by following the gas evolution profiles achieved at 75 ºC. For that, 0.15 g of catalyst was placed in a reactor with 5 mL of distilled water and, after purging the system with nitrogen gas, 5 mL of a solution containing formic acid/sodium formate 2M with a molar ratio of 9/1 was incorporated. The reactor was connected to a burette system so that the total gas generated could be measured. For the recyclability tests, the catalyst was recovered after the reaction, it was filtered, washed and dried, and its activity was assessed under identical reaction conditions.

The initial TOF values (h^{-1}) were calculated by the following equation:

$$\mathrm{TOF}\ (\mathrm{h}^{-1}) = \frac{\text{produced } \mathrm{H_2}\ (\text{mole})}{\text{Pd atoms (mole)} \times \text{time (h)}}$$

where the produced H_2 (mole) is the mole of H_2 obtained after 3 min of reaction, and Pd atoms are determined from the Pd content obtained by ICP-OES analysis.

Supporting Information

Acknowledgements

This work is part of the R+D+I project PID2021-123079OB-I00 funded by MCIN/AEI/ 10.13039/501100011033 and by "ERDF A way of making Europe" and also the project TED2021-131324B-C22 funded by MCIN/AEI/ 10.13039/501100011033 and by the "European Union NextGenerationEU/PRTR. MNG would like to thank the grant RYC2021-034199-I funded by MCIN/AEI/ 10.13039/501100011033 and by "ESF Investing in your future".

Keywords: Hydrogen • Formic acid • Biomass residues • PdAg alloy • Nitrogen functional groups

References

[1] M. Navlani-García, K. Mori, Y. Kuwahara, H. Yamashita, *NPG Asia Materials* **2018**, *10*, 277–292.

[2] M. Niermann, A. Beckendorff, M. Kaltschmitt, K. Bonhoff, *Int J Hydrogen Energy* **2019**, *44*, 6631–6654.

[3] C. Kim, Y. Lee, K. Kim, U. Lee, *Catalysts* **2022**, *12*, 1113.

[4] A. Wang, P. He, J. Wu, N. Chen, C. Pan, E. Shi, H. Jia, T. Hu, K. He, Q. Cai, R. Shen, *Energy & Fuels* **2023**, *37*, 17075–17093.

[5] D. A. Bulushev, *Energies* **2021**, *14*, 1334.

[6] D. A. Bulushev, L. G. Bulusheva, *Catalysis Reviews* **2022**, *64*, 835–874.

[7] M. Navlani-García, K. Mori, D. Salinas-Torres, Y. Kuwahara, H. Yamashita, *Front Mater* **2019**, *6*, 439363.

[8] M. Navlani-García, D. Salinas-Torres, D. Cazorla-Amorós, *Energies* **2019**, *12*, 4027.

[9] M. Navlani-García, K. Mori, A. Nozaki, Y. Kuwahara, H. Yamashita, *Ind Eng Chem Res* **2016**, *55*, 7612–7620.

[10] M. Wen, K. Mori, Y. Futamura, Y. Kuwahara, M. Navlani-García, T. An, H. Yamashita, *Scientific Reports* **2019**, *9*, 1–10.

[11] K. Mori, M. Dojo, H. Yamashita, *ACS Catal* **2013**, *3*, 1114–1119.

[12] S. Wan, P. Lu, D. Xu, V. Valtchev, *Catal Commun* **2024**, 106891.

[13] K. Mori, T. Fujita, H. Yamashita, *EES Catalysis* **2023**, *1*, 84–93.

[14] J. Chaparro-Garnica, M. Navlani-García, D. Salinas-Torres, E. Morallón, D. Cazorla-Amorós, *ACS Sustain Chem Eng* **2020**, *8*, 15030–15043.

[15] M. Navlani-García, K. Mori, A. Nozaki, Y. Kuwahara, H. Yamashita, *ChemistrySelect* **2016**, *1*, 1879–1886.

[16] C. Martin, A. Quintanilla, G. Vega, J. A. Casas, *Appl Catal B* **2022**, *317*, 121802.

[17] J. L. Santos, C. Megías-Sayago, S. Ivanova, M. Á. Centeno, J. A. Odriozola, *Chemical Engineering Journal* **2021**, *420*, 127641.

[18] H. jin Jeon, Y. M. Chung, *Appl Catal B* **2017**, *210*, 212–222.

[19] M. Navlani-García, D. Salinas-Torres, F. D. Vázquez-Álvarez, D. Cazorla-Amorós, *Catal Today* **2022**, 428–435.

[20] A. Ortega-Murcia, M. Navlani-García, E. Morallón, D. Cazorla-Amorós, *Front Chem* **2020**, *8*, 534710.

[21] M. R. Nabid, Y. Bide, B. Etemadi, *New Journal of Chemistry* **2017**, *41*, 10773–10779.

[22] Y. Kim, H. Lee, S. Yang, J. Lee, H. Kim, S. Hwang, S. W. Jeon, D. H. Kim, *J Catal* **2021**, *404*, 324–333.

[23] Y. Kim, D. H. Kim, *Appl Catal A Gen* **2020**, *608*, 117887.

[24] Z. Zhang, Y. Luo, S. Liu, Q. Yao, S. Qing, Z. H. Lu, *J Mater Chem A Mater* **2019**, *7*, 21438–21446.

[25] J. Sun, H. Qiu, W. Cao, H. Fu, H. Wan, Z. Xu, S. Zheng, *ACS Sustain Chem Eng* **2019**, *7*, 1963–1972.

[26] S. Masuda, K. Mori, Y. Futamura, H. Yamashita, *ACS Catal* **2018**, *8*, 2277–2285.

[27] Y. Wu, Y. Li, X. Chen, G. Li, H. Huang, L. Jia, *Ind Eng Chem Res* **2021**, *60*, 12265–12274.

[28] C. Wan, F. Yao, X. Li, K. Hu, M. Ye, L. Xu, Y. An, *ChemistrySelect* **2016**, *1*, 6907–6913.

[29] M. Navlani-García, D. Salinas-Torres, K. Mori, Y. Kuwahara, H. Yamashita, *Int J Hydrogen Energy* **2019**, *44*, 28483–28493.

[30] Y. Wu, M. Wen, M. Navlani-García, Y. Kuwahara, K. Mori, H. Yamashita, *Chem Asian J* **2017**, *12*, 860–867.

[31] J. Chaparro-Garnica, M. Navlani-García, D. Salinas-Torres, E. Morallón, D. Cazorla-Amorós, *Materials* **2021**, *14*, 6506.

[32] J. Chaparro-Garnica, M. Navlani-García, D. Salinas-Torres, Á. Berenguer-Murcia, E. Morallón, D. Cazorla-Amorós, *Fuel* **2022**, *320*, 123900.

[33] J. M. V. Nabais, C. E. C. Laginhas, P. J. M. Carrott, M. M. L. Ribeiro Carrott, *Fuel Processing Technology* **2011**, *92*, 234–240.

[34] J. Chaparro-Garnica, M. Guiton, D. Salinas-Torres, E. Morallón, E. Benetto, D. Cazorla-Amorós, *J Clean Prod* **2022**, *380*, 135098.

[35] Z. Ruiz-Bernal, M. Á. Lillo-Ródenas, M. C. Román-Martínez, *Catalysts* **2021**, *11*, 559.

[36] F. Quesada-Plata, R. Ruiz-Rosas, E. Morallón, D. Cazorla-Amorós, *Chempluschem* **2016**, *81*, 1349–1359.

[37] K. Mandal, D. Bhattacharjee, S. Dasgupta, *Int J Hydrogen Energy* **2015**, *40*, 4786–4793.

[38] H. Liu, Y. Guo, Y. Yu, W. Yang, M. Shen, X. Liu, S. Geng, J. Li, C. Yu, Z. Yin, H. Li, *J Mater Chem A Mater* **2018**, *6*, 17323–17328.

[39] Y. Kim, D. H. Kim, *Molecular Catalysis* **2023**, *547*, 113343.

[40] I. Coulthard, T. K. Sham, *Phys Rev Lett* **1996**, *77*, 4824.

[41] M. Navlani-García, D. Salinas-Torres, K. Mori, A. F. Léonard, Y. Kuwahara, N. Job, H. Yamashita, *Catal Today* **2019**, *324*, 90–96.

[42] Q. Lv, Q. Meng, W. Liu, N. Sun, K. Jiang, L. Ma, Z. Peng, W. Cai, C. Liu, J. Ge, L. Liu, W. Xing, *Journal of Physical Chemistry C* **2018**, *122*, 2081–2088.

[43] O. Y. Podyacheva, D. A. Bulushev, A. N. Suboch, D. A. Svintsitskiy, A. S. Lisitsyn, E. Modin, A. Chuvilin, E. Y. Gerasimov, V. I. Sobolev, V. N. Parmon, *ChemSusChem* **2018**, *11*, 3724–3727.

[44] D. A. Bulushev, M. Zacharska, E. V. Shlyakhova, A. L. Chuvilin, Y. Guo, S. Beloshapkin, A. V. Okotrub, L. G. Bulusheva, *ACS Catal* **2016**, *6*, 681–691.

[45] Q. Y. Bi, J. D. Lin, Y. M. Liu, H. Y. He, F. Q. Huang, Y. Cao, *Angewandte Chemie International Edition* **2016**, *55*, 11849–11853.

[46] J. Chen, M. Yang, M. Pang, F. Gao, P. Guo, *Colloids Surf A Physicochem Eng Asp* **2021**, *629*, 127404.

[47] N. Benipal, J. Qi, Q. Liu, W. Li, *Appl Catal B* **2017**, *210*, 121–130.

[48] Y. Holade, C. Morais, S. Arrii-Clacens, K. Servat, T. W. Napporn, K. B. Kokoh, *Electrocatalysis* **2013**, *4*, 167–178.

[49] X. Liu, C. Dai, D. Wu, A. Fisher, Z. Liu, D. Cheng, *Chem Lett* **2016**, *45*, 732–734.

[50] Y. Ping, J. M. Yan, Z. L. Wang, H. L. Wang, Q. Jiang, *J Mater Chem A Mater* **2013**, *1*, 12188–12191.

[51] L. Yang, X. Hua, J. Su, W. Luo, S. Chen, G. Cheng, *Appl Catal B* **2015**, *168*, 423–428.

[52] Q. F. Deng, J. J. Xin, S. K. Ma, F. J. Cui, Z. L. Zhao, L. H. Jia, *Energy Technology* **2018**, *6*, 2374–2379.

[53] C. Feng, S. Gao, N. Shang, X. Zhou, C. Wang, *Energy Technology* **2018**, *6*, 2120–2125.

[54] X. Zhang, N. Shang, X. Zhou, C. Feng, S. Gao, Q. Wu, Z. Wang, C. Wang, *New Journal of Chemistry* **2017**, *41*, 3443–3449.

[55] F. Yao, X. Li, C. Wan, L. Xu, Y. An, M. Ye, Z. Lei, *Appl Surf Sci* **2017**, *426*, 605–611.

[56] X. Zhang, N. Shang, H. Shang, T. Du, X. Zhou, C. Feng, S. Gao, C. Wang, Z. Wang, *Energy Technology* **2019**, *7*, 140–145.

[57] A. Bulut, M. Yurderi, Y. Karatas, Z. Say, H. Kivrak, M. Kaya, M. Gulcan, E. Ozensoy, M. Zahmakiran, *ACS Catal* **2015**, *5*, 6099–6110.

[58] H. Dai, N. Cao, L. Yang, J. Su, W. Luo, G. Cheng, *J Mater Chem A Mater* **2014**, *2*, 11060–11064.

[59] S. T. Gao, W. Liu, C. Feng, N. Z. Shang, C. Wang, *Catal Sci Technol* **2016**, *6*, 869–874.

[60] I. Such-Basáñez, M. C. Román-Martínez, C. S. M. De Lecea, *Carbon* **2004**, *42*, 1357–1361